Optimum Source Design for Detection of Heterogeneities in Diffuse Optical Imaging

Ahmed Serdaroglu[a], Birsen Yazici[a], and Kiwoon Kwon[a]

[a]Department of Electrical, Computer, and Systems Engineering, Rensselaer Polytechnic Institute, 110 8th Street, Troy, NY, USA 12180

ABSTRACT

This work investigates the design of optimum distribution of photon density power among the source positions, and modulation frequencies to maximize the detectability of heterogeneities in near-infrared diffuse optical tomography. We start our analysis by first deriving the discrete source-to-detector map based on the finite-element formulation of the frequency-domain diffusion equation with Robin boundary conditions. We formulate the detection of heterogeneities with respect to a given background as a hypothesis testing problem and use signal-to-noise ratio (SNR) of the test statistics as a figure of merit for detectability. We, next, maximize the SNR of the test statistics with respect to the source power distributed over a predetermined set of locations and frequencies. When the optimal linear detector is used for detection, optimal source power distribution is given as the maximum eigenfunction of the source-to-detector map normalized with respect to the covariance of measurement noise. We present numerical studies to demonstrate the performance of our approach with respect to number of source locations, tumor size, and tumor location.

Keywords: Waveform design, tumor detection, diffuse optical tomography, optimum source design

1. INTRODUCTION

Diffuse optical imaging in the near infra-red (NIR) region has emerged as an important tool for chemical, biological and molecular sensing and imaging. Diffuse optical imaging involves reconstruction of spatially varying optical properties of turbid medium, as well as fluorophore lifetime and yield from boundary measurements based on a photon propagation model. In most biomedical applications, NIR light at different wavelengths and modulation frequencies is transmitted into the domain at the surface from a set of source locations, and the exiting light is measured by a set of detectors on the boundary. In typical diffuse optical tomography (DOT) systems, light source is time-multiplexed between different wavelengths, modulation frequencies, and source locations. This leads to slower data acquisition and low temporal resolution which may be limiting in many applications, such as pharmacokinetic analysis of optical contrast agents and functional brain imaging. Currently, high temporal resolution DOT systems employing sophisticated multiplexing schemes are under development. These systems, unlike time-multiplexed systems, transmit all wavelengths and modulation frequencies simultaneously from all sources. Piao *et al.* formed the source-detector coupling of the tomographic measurements where all the sources emit light simultaneously, by wavelength multiplexing the emitted source intensities.[1] There also exits optical imaging systems where the tissue dynamics and chromophore concentrations are explored based on multi-wavelength measurements.[2–5] Bevilacqua *et al.* developed a combined frequency domain (FD) and continuous wave (CW) system for absorption spectroscopy.[6] Corlu *et al.* investigated the optimal choice of wavelengths for a multispectral CW DOT problem to maximize the separability of the wavelength-independent concentrations of chromophores..[7]

This paper investigates optimal distribution of allowable source power over a predetermined set of source locations and modulation frequencies for such systems. Our analysis is also applicable to those fast dynamic systems which employ detectors with limited dynamic range. The optimization of system parameters in diffuse optical imaging has been investigated by a number of researchers to maximize resolution and reconstruction quality. Graves *et al.* performed an experimental study where the number and location of sources and detectors

Further author information: (Send correspondence to Ahmed Serdaroglu)
E-mail: serdaa2@rpi.edu, Telephone: 1 518 276 6085

Optical Methods for Tumor Treatment and Detection: Mechanisms and Techniques in Photodynamic Therapy XV, edited by David Kessel, Proc. of SPIE Vol. 6139, 61391A, (2006) · 1605-7422/06/$15 · doi: 10.1117/12.647209

are optimized by comparing the singular-value spectra of the weight matrices obtained from the forward problem solution of the fluorescence molecular tomography system under various choices of parameters.[8] Xu *et al.* investigated the optimal location of optical fibers for a hybrid magnetic resonance imaging (MRI) and NIR imaging system such that the maximum possible resolution is obtained in small animal studies.[9] Oh *et al.* explored the calibration of source and detector coupling coefficients.[10] There exists diffuse optical imaging systems where a set of different modulation frequencies are applied in order to increase the amount of data and to be able to obtain better reconstructions of the absorption and/or diffusion coefficients inside the domain.[11,12]

Similar studies have been reported for the design of optimal current patterns to maximize the detectability of heterogeneities in electrical impedance tomography (EIT) images. EIT is concerned with the reconstruction of the conductivity of a medium given current sources and voltage boundary measurements. In,[13] Isaacson proposed a distinguishability criterion based on L^2 norm for EIT such that the norm of the difference between the voltage readings corresponding to the heterogeneity-present and heterogeneity-absent cases is maximized constrained by the constant current determined by health limits. This study showed that best current pattern is given by the eigenfunctions of the difference between the resistance matrices that maps source current to boundary voltage obtained by the detector readings. Optimum current patterns in EIT have been designed by several researchers.[14–16]

In this work, we explore the design of optimal distribution of source power over a predetermined set of source locations and modulation frequencies to maximize detection of heterogeneities in a turbid medium. The detection task involves maximizing the contrast of heterogeneities with respect to a background. We start our analysis with the derivation of the source-to-detector map based on the finite element method (FEM) discretization of the diffusion equation with Robin boundary condition. We next formulate the detection of heterogeneities in a given background as a hypothesis testing problem and use optimal linear detector and SNR of the test statistics as a figure of merit for detectability.[17] Under the assumption of linear detection (or Gaussian data) and white additive noise, our figure of merit for detectability is equivalent to the distinguishability criterion given in.[13] Optimal distribution of source power is given by the eigenfunctions of the normalized difference of the source-to-detector maps when a heterogeneity is absent and present.

The rest of the paper is organized as follows: In Section 2, we derive source-to-detector map. In Section 3, we present the statistical formulation of the detection problem, introduce SNR of the test statistics as a figure of merit, and derive optimal source power distribution. In Section 4, we present simulation results. Finally, Section 5 concludes our work.

2. SOURCE-TO-DETECTOR MAP FOR DIFFUSE OPTICAL TOMOGRAPHY

Diffuse optical tomography involves recovery of spatially varying optical absorption and scattering coefficients in the interior of a domain Ω from measurements of transmitted light on the boundary $\partial\Omega$ based on a photon propagation model.[18] Radiation transport equation (RTE) provides a general mathematical model for the photon propagation. However, in scattering dominant medium, diffusion approximation to RTE is a sufficient model for the propagation of NIR light. In frequency-domain, diffusion equation with Robin boundary conditions is given by:

$$-\nabla D(r)\nabla\Phi(r,\omega) + \left(\mu_a(r) + \frac{i\omega}{c}\right)\Phi(r,\omega) = S(r,\omega) \qquad \text{in } \Omega \tag{1a}$$

$$\Phi(\zeta) + 2AD(\zeta)\frac{\partial\Phi(\zeta,\omega)}{\partial\nu} = 0 \qquad \text{on } \partial\Omega \tag{1b}$$

where $D(r)$ is the diffusion coefficient given by $D(r) = \frac{1}{3[\mu_s'(r)+\mu_a(r)]}$, $\mu_a(r)$ and $\mu_s'(r)$ are the absorption and reduced scattering coefficients, $S(r,\omega)$ and $\Phi(r,\omega)$ are the optical source term and the photon density at position r and modulation frequency ω. $A = (1+R)/(1-R)$ with R being the refraction index parameter at the boundary, ζ is the spatial position on $\partial\Omega$, and ν is the outer normal unit vector on $\partial\Omega$.[19]

The actual measurements at a position $r = \zeta$ on $\partial\Omega$ is the exitance $\Gamma(\zeta,\omega)$ given by:

$$\Gamma(\zeta,\omega) = -D(\zeta)\frac{\partial\Phi(\zeta,\omega)}{\partial\nu} = \xi(\zeta)\Phi(\zeta,\omega), \tag{2}$$

where $\xi = 1/2A$. Note that the second equality comes from Robin boundary condition (1b).

The diffusion equation (1) can be discretized by using finite element method (FEM). In FEM, the solution, Φ, is approximated by a piecewise polynomial as follows:

$$\Phi(r,\omega) = \sum_{i=1}^{N_n} \phi_i(\omega)u_i(r), \tag{3}$$

where u_i are basis functions with compact support spanning a finite dimensional subspace of an associated Sobolev space[20] and N_n is the number of vertex nodes. Note that for a piecewise linear or piecewise bilinear element, N_n is equal to the number of nodes.

Galerkin method results in the following systems of equations:

$$[\mathbf{K} + \mathbf{C} + \mathbf{A}]\,\mathbf{\Phi} = \mathbf{V}\mathbf{\Phi} = \mathbf{b}, \tag{4}$$

where $\mathbf{K}, \mathbf{C}, \mathbf{A}$ are $N_n \times N_n$ matrices, $\mathbf{\Phi}$ is a vector containing the photon densities at each node, and $\mathbf{b}$ is an $N_n \times 1$ column vector corresponding to the source terms at each node. The elements of $\mathbf{K}, \mathbf{C}, \mathbf{A}$, and $\mathbf{b}$ are given by:

$$\begin{aligned}
\mathbf{K}_{kl} &= \int_\Omega D(r)\nabla u_k(r)\nabla u_l(r)d^n r, \\
\mathbf{C}_{kl} &= \int_\Omega \left(\mu_a(r) + \frac{i\omega}{c}\right) u_k(r)u_l(r)d^n r, \\
\mathbf{A}_{kl} &= \int_{\partial\Omega} \xi u_k(r)u_l(r)d^{n-1} r, \\
\mathbf{b}_l &= \int_{\partial\Omega} S(r,\omega)u_l(r)d^n r,
\end{aligned} \tag{5}$$

for $k, l = 1, \cdots, N_n$.

Since the left hand side of (4) is in coercive continuous bilinear form in $H^1(\Omega) \times H^1(\Omega)$ and the right hand side of (4) is a linear functional on $H^1(\Omega)$, (4) has a unique solution Φ_{N_n} in the finite element space V_{N_n} by Lax-Milgram lemma.[20]

The vector $\mathbf{b}$ in (4) denotes the source values at each node of the finite element mesh. Therefore, it is a sparse vector. $\mathbf{b}$ can be reduced to the $N_s \times 1$ vector which is composed of the source values at the source positions for a fixed modulation frequency ω_l given by:

$$\mathbf{s}_l = \mathbf{P}_s^{-1}\mathbf{b}, \tag{6}$$

where $\mathbf{P}_s$ is an $N_n \times N_s$ matrix given by:

$$\mathbf{P}_s(j,k) = \begin{cases} 1 & \text{if the position of the } k\text{-th source is the } j\text{-th node,} \\ 0 & \text{otherwise} \end{cases} \tag{7}$$

For this study, we assume that the source power $S(r,\omega)$ is distributed over a set predetermined locations $r_k, k = 1, \cdots, N_s$ and modulation frequencies $\omega_l, l = 1, \cdots, N_\omega$.

$$S(r,\omega) = \sum_{k=1}^{N_s} \sum_{l=1}^{N_\omega} s_{kl}\delta(r - r_k)\delta(\omega - \omega_l), \tag{8}$$

where N_s is the number of sources, N_ω is the number of modulation frequencies, and s_{kl} denotes the peak amplitude of the photon density at location r_k and modulation frequency ω_l.

From (8), we form the following vector:

$$\mathbf{s}_l = \left[s_{1l}, s_{2l}, \cdots, s_{N_s l}\right]^T, \tag{9}$$

for $l = 1, \cdots, N_\omega$. We shall refer to $\mathbf{s}_l$, whose elements are derived from (6), as the source vector at frequency ω_l. Source vector can be obtained numerically from the FEM solution given in (5).

The measurements at the boundary, $\mathbf{\Phi}_d$, can be obtained by

$$\mathbf{\Phi}_d = \mathbf{P}_d \mathbf{\Phi}, \tag{10}$$

where $\mathbf{P}_d$ is an $N_d \times N_n$ matrix given by:

$$\mathbf{P}_d(i,j) = \begin{cases} \xi(i) & \text{if the position of the } i\text{-th detector is the } j\text{-th node,} \\ 0 & \text{otherwise} \end{cases} \tag{11}$$

where $i = 1, \cdots, N_d; \quad j = 1, \cdots, N_n; \quad k = 1, \cdots, N_s$; N_d is the number of detectors; and $\xi(i)$ is the reflection coefficient at the i-th detector.

We shall refer to the matrix which maps the source values to the detector readings as *source-to-detector* map. This map is given by

$$\mathbf{\Lambda} = \mathbf{P}_d \mathbf{V}^{-1} \mathbf{P}_s. \tag{12}$$

In general, $\mathbf{\Lambda}$ depends on both the spatially varying absorption coefficients, $\boldsymbol{\mu}_a$, and diffusion coefficients, $\mathbf{D}$, at each node of the finite element mesh. In this paper, we assume that the diffusion coefficient is known and constant throughout the domain; and therefore, $\mathbf{\Lambda}$ depends only on $\boldsymbol{\mu}_a$. Extension of the analysis to the case of unknown D is straightforward and will be omitted for notational clarity. We will denote the source-to-detector map by $\mathbf{\Lambda}(\boldsymbol{\mu}_a)$ for the rest of the paper.

With the definition of the source-to-detector map given in (12), the relation between the ideal measurements, $\mathbf{\Phi}_d$, and sources, $\mathbf{s}$, is given by:

$$\mathbf{\Phi}_d = \mathbf{\Lambda}(\boldsymbol{\mu}_a)\mathbf{s}_l. \tag{13}$$

To simplify our notation, for the rest of the paper, we shall drop l and simply write $\mathbf{s}$ instead of $\mathbf{s}_l$.

3. DETECTION OF HETEROGENEITIES IN DIFFUSE OPTICAL IMAGING

The source-to-detector relationship given in (13) is an ideal model; however, in practice, diffuse optical measurements contain additive thermal noise. Therefore, a more realistic representation of the measurement model is given by:

$$\mathbf{d} = \mathbf{\Lambda}(\boldsymbol{\mu}_a)\mathbf{s} + \mathbf{n}, \tag{14}$$

where $\mathbf{n}$ is the measurement noise vector. Note that the raw measurements may be transformed by a transformation $\mathcal{M}$ before reconstruction. As long as $\mathcal{M}$ is a linear operator, the analysis remains the same. Therefore, without loss of generality, we assume that (14) is the measurement model.

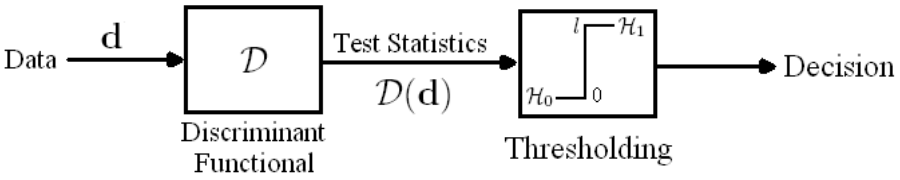

Figure 1. Block diagram of a detector.

The problem of detecting a heterogeneity embedded in a background can be viewed as the classical problem of binary hypothesis testing[17] where the absorption coefficients at each node of the finite element mesh, $\boldsymbol{\mu}_a$ are classified into one of the two categories: (i) resulting from a background without a tumor, or (ii) due to a domain with a tumor embedded in the background.

Let $\boldsymbol{\mu}_{a0}$ denote the absorption coefficient of the background of a medium at every node of the FEM mesh. Similarly, let $\boldsymbol{\mu}_{a1}$ denote the absorption coefficient of the same medium with a heterogeneity embedded in the background. A statistical decision strategy can be developed to choose one of the following hypotheses given the measurements:

$$\begin{aligned} \mathcal{H}_0 &: \mathbf{d} = \mathbf{\Lambda}(\boldsymbol{\mu}_{a0})\mathbf{s} + \mathbf{n} \Longrightarrow \text{heterogeneity is absent,} \\ \mathcal{H}_1 &: \mathbf{d} = \mathbf{\Lambda}(\boldsymbol{\mu}_{a1})\mathbf{s} + \mathbf{n} \Longrightarrow \text{heterogeneity is present.} \end{aligned} \tag{15}$$

where $\mathcal{H}_0$ is called the null hypothesis, and $\mathcal{H}_1$ is called the alternative hypothesis.

Mathematical formulation of the hypothesis testing problem leads to a detector structure which is composed of two elements: a discriminant functional $\mathcal{D}$ and a threshold value, l. The discriminant functional is a mapping from the measurement vector, $\mathbf{d} \in \mathbb{C}^N$ to $\mathbb{R}$. $\mathcal{D}(\mathbf{d})$ is referred as the *test statistics*. Comparison of $\mathcal{D}(\mathbf{d})$ to the threshold, l, leads to acceptance of either $\mathcal{H}_0$ or $\mathcal{H}_1$. Figure 1 shows the block diagram of a detector.

In general, the discriminant functional can be derived from the Neyman-Pearson criterion.[17] Let $\mathrm{p}(\mathbf{d}|\mathcal{H}_0)$ and $\mathrm{p}(\mathbf{d}|\mathcal{H}_1)$ denote the conditional probability density functions of the measurements under the null and alternative hypotheses, respectively. Then one can show that:

$$\mathcal{D}(\mathbf{d}) = \log\, \mathrm{p}(\mathbf{d}|\mathcal{H}_1) - \log\, \mathrm{p}(\mathbf{d}|\mathcal{H}_0). \tag{16}$$

In general, the test statistic given by (16), leads to nonlinear discriminant functionals, if the conditional probability density functions are not Gaussian with equal covariance matrices. In this study, however, we consider detectors that are optimal amongst all detectors. A linear detector leads to a discriminant functional that is linear in data. Linear discriminant functionals are easy to compute, their performance is easy to summarize, and far less information regarding the data statistics is needed in designing a linear detector. Linear discriminants have the general form:

$$\mathcal{D}(\mathbf{d}) = \mathbf{d}^T\mathbf{w}, \tag{17}$$

where $\mathbf{w}$ is the so-called template function chosen to minimize a *measure of detectability* .[17]

Clearly, the fraction of true and false decisions depend on the decision threshold, l. By varying the decision threshold, l, and plotting the fraction of true decisions versus fraction of false decisions, one can obtain the so-called receiver (detector) operating characteristics (ROC) curve. ROC curve is a very useful tool, because, it summarizes the performance of the decision strategy. One of the important figures of merit derived from ROC is the area under the ROC curve or AUC. In general, the degree of the overlap of the probability density functions of the test statistics under two decisions determines the detectability of a heterogeneity. AUC is a good measure of this overlap. However, it is often times not a practical figure of merit for optimization problems. An alternative figure of merit is given by the SNR of the test statistics defined as:

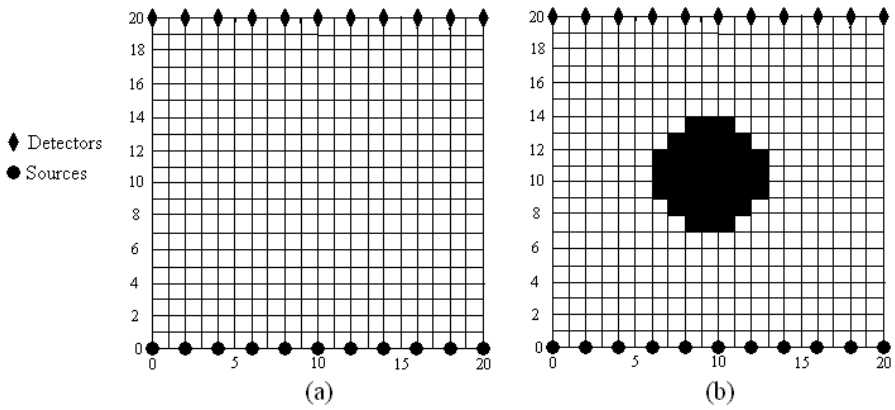

Figure 2. The finite element mesh used for (a) a homogeneous background, and (b) a tumor embedded domain.

$$\mathrm{SNR}_{\mathcal{D}(\mathbf{d})} = \frac{\left(E\left[\mathcal{D}(\mathbf{d})|\mathcal{H}_1\right] - E\left[\mathcal{D}(\mathbf{d})|\mathcal{H}_0\right]\right)^2}{Var\left[\mathcal{D}(\mathbf{d})|\mathcal{H}_1\right] + Var\left[\mathcal{D}(\mathbf{d})|\mathcal{H}_0\right]}, \tag{18}$$

where $E[\cdot]$ denotes expectation, and $Var[\cdot]$ denotes variance.

Among all linear detectors, the Hotelling detector, also known as the Fisher detector,[21] is the optimal detector. The Hotelling detector maximizes the SNR of the test statistic given in (18).

Hotelling detector uses the first and second order statistics of the data to calculate the template function, $\mathbf{w}$. The template function for a Hotelling detector is given by:

$$\mathbf{w} = \mathbf{C}^{-1}\Delta\mathbf{m}, \tag{19}$$

In (19), $\mathbf{C} = (\mathbf{C}_0 + \mathbf{C}_1)/2$ and $\Delta\mathbf{m} = \mathbf{m}_1 - \mathbf{m}_0$, where $\mathbf{C}_i$ & $\mathbf{m}_i, i = 0, 1$ are the conditional covariance matrices and mean vectors of the data under hypothesis $\mathcal{H}_i, i = 0, 1$, respectively. The SNR of the test-statistics for the Hotelling detector is given by:

$$\mathrm{SNR}_{\mathcal{D}(\mathbf{d})} = \|\Delta\mathbf{m}\|^2_{\mathbf{C}^{-1}}, \tag{20}$$

where $\|\Delta\mathbf{m}\|^2_{\mathbf{C}^{-1}} = \Delta\mathbf{m}^T\mathbf{C}^{-1}\Delta\mathbf{m}$.

In this study, we assume that $\boldsymbol{\mu}_{a0}$ and $\boldsymbol{\mu}_{a1}$ in (15) are deterministic quantities. Therefore, the random nature of the data comes from the additive noise term only.

Assuming that the noise vector $\mathbf{n}$ is a zero-mean Gaussian random vector with covariance matrix $\mathbf{C}$, the measurements are also represented by Gaussian densities, with conditional mean vectors given as $\boldsymbol{\Lambda}(\boldsymbol{\mu}_{a0})\mathbf{s}$, and $\boldsymbol{\Lambda}(\boldsymbol{\mu}_{a1})\mathbf{s}$, for the null and alternative hypotheses, respectively. The conditional covariance matrix under the two hypotheses is the same and given by $\mathbf{C}$. Inserting the conditional mean vectors and the conditional covariance matrix into (19), the following test statistics is obtained:

$$\mathcal{D}(\mathbf{d}) = \mathbf{d}^T\mathbf{C}^{-1}\left[\boldsymbol{\Lambda}(\mu_{\mathbf{1}}) - \boldsymbol{\Lambda}(\mu_{\mathbf{0}})\right]\mathbf{s} \tag{21}$$

Our objective is to obtain the optimum source vector maximizing the $\mathrm{SNR}_{\mathcal{D}(\mathbf{d})}$ given in (18). By (20), the SNR can be rewritten as follows:

$$\mathrm{SNR}_{\mathcal{D}(\mathbf{d})} = \|\left[\boldsymbol{\Lambda}(\boldsymbol{\mu}_1) - \boldsymbol{\Lambda}(\boldsymbol{\mu}_0)\right]\mathbf{s}\|^2_{\mathbf{C}^{-1}}. \tag{22}$$

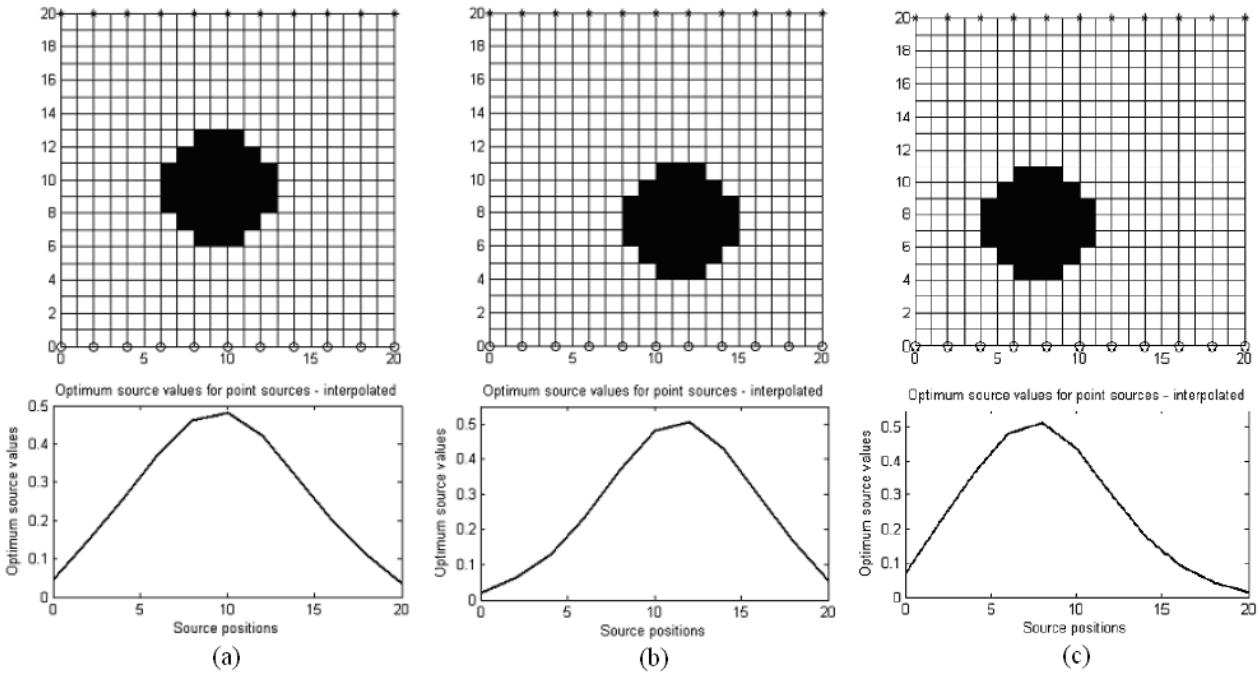

Figure 3. Optimum source values plotted with respect to source positions. (a) Tumor location is (3cm,3cm). $\lambda = 1.35 \times 10^{-9}$ (b) Tumor location is (3.6cm,2.4cm). $\lambda = 1.35 \times 10^{-9}$ (c) Tumor location is (2.4cm,2.4cm). $\lambda = 1.30 \times 10^{-9}$

Clearly, the source vector which maximizes $\mathrm{SNR}_{\mathcal{D}(\mathbf{d})}$ is the *eigenvector* corresponding to the maximum eigenvalue of the matrix

$$\boldsymbol{\Upsilon} = \left[\boldsymbol{\Lambda}(\boldsymbol{\mu}_1) - \boldsymbol{\Lambda}(\boldsymbol{\mu}_0)\right]^T \mathbf{C}^{-1} \left[\boldsymbol{\Lambda}(\boldsymbol{\mu}_1) - \boldsymbol{\Lambda}(\boldsymbol{\mu}_0)\right]. \tag{23}$$

with the constraint given by $\|\mathbf{s}\|^2 = E_s$. This constraint is imposed by the fact that there is a health limit for the amount of light power, E_s, that can be transmitted into the tissue. Without loss of generality, we assume that E_s is equal to 1 in our numerical simulations. The optimum source energies must be scaled with the appropriate power limit term according to the tissue type and experimental standards.[22]

The maximum eigenvalue of $\boldsymbol{\Upsilon}$ is the maximum SNR, value which determines the amount of detectability of the tumor, and is denoted by λ for the rest of the paper.

4. NUMERICAL EXPERIMENTS

The numerical experiments performed in this work can be grouped into two categories. In the first set of experiments, we assume that the sources are modulated at a single frequency. Therefore, we determine the optimal distribution of source power over a predetermined set of source locations. We investigate the effect of tumor location, tumor size, and the number of source locations on the optimum source vales. The detectability is measured by the maximum eigenvalue, λ, of the matrix $\boldsymbol{\Upsilon}$ given by equation (23), where $\mathbf{C}$ is set to be the identity matrix. In the second set of experiments, we investigate the optimal distribution of source power over a predetermined set of modulation frequencies.

4.1. Optimum distribution of source power over a set of source locations

We choose the finite-element mesh shown in Figure 2 for our first set of experiments. The domain is 6cm× 6cm, and the tumor radius is 1cm. The FEM mesh is 20×20 which provides a resolution of 3mm in both directions. There are 11 sources that are equally spaced in the lower boundary of the domain. The corresponding

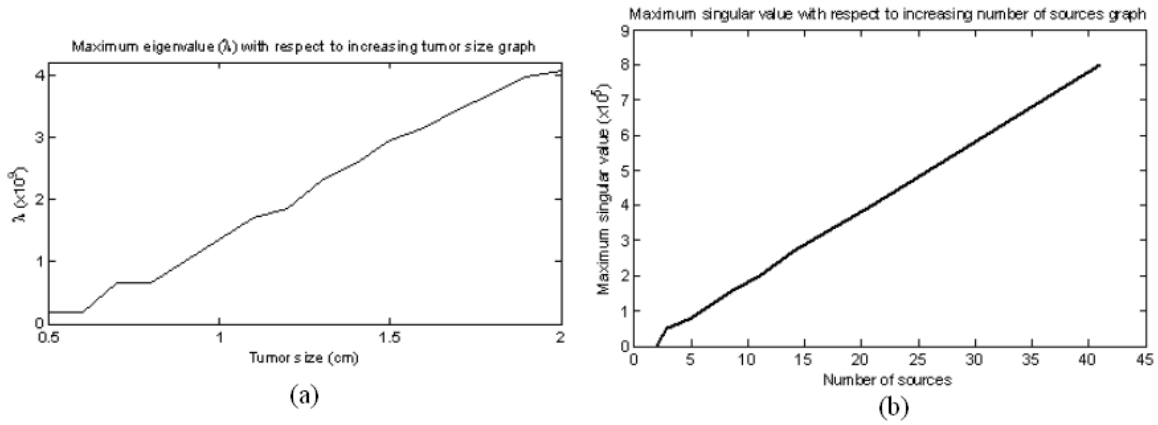

Figure 4. (a) Maximum eigenvalue, λ, with respect to tumor size graph. (b) Maximum singular value of $\mathbf{\Lambda}(\boldsymbol{\mu}_1) - \mathbf{\Lambda}(\boldsymbol{\mu}_0)$ with respect to the number of sources graph.

detectors are located symmetrically to the opposite side of the source boundary, namely the upper boundary. The modulation frequency is set to 500 MHz. The background absorption coefficient, the absorption coefficient of the heterogeneity, and the reduced scattering coefficient throughout the medium, are chosen as $\mu_{a0} = 0.05\text{cm}^{-1}$, $\mu_{a1} = 0.2\text{cm}^{-1}$, and $\mu_s' = 8\text{cm}^{-1}$, respectively. The vector representing the optimum source values is:

$$\mathbf{s} = [s_1, s_2, \ldots, s_{11}]^T. \tag{24}$$

Our objective is to find the optimum value of the vector $\mathbf{s}$, which is the eigenvector of the matrix $\mathbf{\Upsilon}$ corresponding to the maximum eigenvalue, λ.

4.1.1. Effect of tumor location with respect to the sources

In this experiment, different tumor locations are chosen within the domain. The results of the experiments are summarized in Figure 3. The optimum source values are plotted for each position and interpolated in between. Note that the maximum eigenvalues are given under each plot to compare the detectability with respect to tumor location. We observe that the maximum entry of the source vector corresponds to the source position where the light photons have to traverse the longest path through the absorbing heterogeneity. Thus, one can optimize the source power distribution based on the position and shape of the tumor which may be estimated *a priori* by using a secondary imaging modality.

4.1.2. Effect of tumor size on detectability

In this experiment, we increase the tumor radius from 0.5cm to 2cm with increments of 0.1cm, and plot the maximum eigenvalues, λ's, with respect to tumor size as shown in Figure 4(a). The tumor is centered at position (3cm, 3cm). The maximum eigenvalue λ, increases with the increasing tumor size. This is expected, since larger tumors are easier to detect as compared to smaller ones. Note that the relationship between the maximum eigenvalue and the tumor size is almost linear.

4.1.3. Effect of number of sources on detectability

In this experiment, we vary the number of sources and detectors to quantify the detectability of a heterogeneity with respect to number of sources and detectors. To obtain a good resolution, the domain is divided into 40×40 pixels. The sources are located such that they are symmetrical with respect to the center of the lower bound of the domain. The tumor is centered at position (3cm, 3cm). Figure 4(b) shows the maximum singular value of $\mathbf{\Lambda}(\boldsymbol{\mu}_1) - \mathbf{\Lambda}(\boldsymbol{\mu}_0)$ versus the number of sources. Clearly, the detectability increases with the increasing numbers of sources. Note that the relationship between the maximum singular value and the number of sources is linear, and quadratic for the maximum eigenvalue.

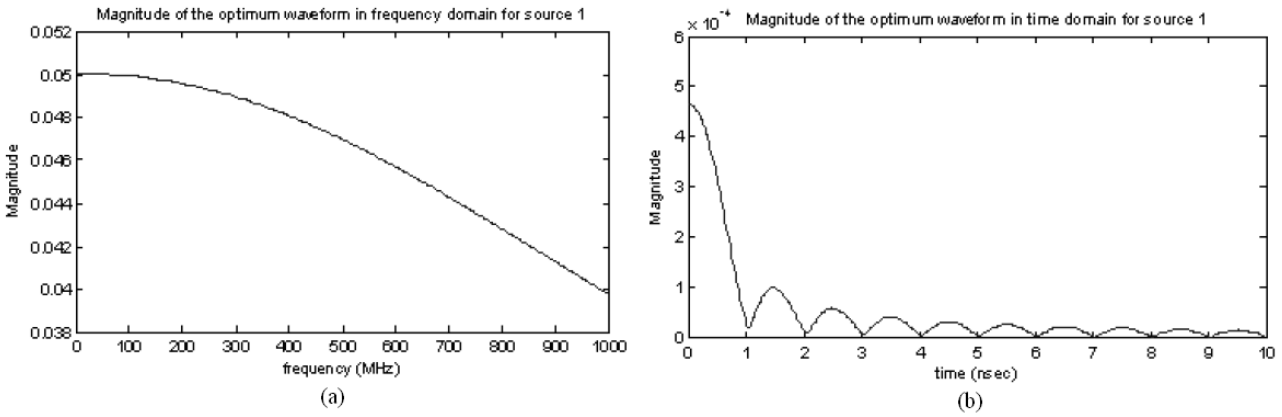

Figure 5. Magnitude of the optimum waveform in frequency-domain (a), and time-domain (b) for source 1

4.2. Optimum distribution of the source power over modulation frequencies

In this experiment, we optimize the distribution of source power over a set of modulation frequencies. The optimum waveform in time-domain is obtained by taking the inverse Fourier transform of the frequency-domain source vector. Since the finite-element algorithm is suitable for solving the frequency-domain diffusion equation given in equation (1a), the optimization of the waveforms is performed in frequency-domain rather than in time-domain. A time-domain analysis can be performed by writing the Backward-Euler algorithm[20] and obtaining the corresponding time-domain source-to-detector map.

We designed the optimum source vector by changing the frequency of the sources from 0Hz to 1GHz with increments of 1MHz and running the finite-element algorithm for each of these frequencies. This provides 1001 source-to-detector matrices each for different frequencies. Similar to equation (9), a source vector corresponding to a frequency ω_l can be defined as:

$$\mathbf{s}_l = [s_{1,l}, s_{2,l}, \ldots, s_{11,l}]^T, \quad \text{for } l = 0, \cdots, 1000. \tag{25}$$

We again use the mesh defined for a domain of size 6cm $\times$ 6cm with the tumor of radius 1cm, centered at position (3cm, 3cm). There are 11 sources, which are ordered from left to right. For example, for the j-th source, we plot the values:

$$[s_{j,0}, s_{j,1}, s_{j,2}, \ldots, s_{j,1000}]^T, \tag{26}$$

with respect to the 1001 frequency values defined as before. Taking the inverse Fourier transform of this vector, we obtain the time-domain optimum waveform for the j-th source. Note that the source values are complex numbers. Figure 5 shows the magnitudes of the optimum waveforms in frequency- and time-domain for the first source. Clearly, the optimum waveform is a low-pass filter as shown in Figure 5(a). In time domain, it is a sinc-like function with the main lobe width being approximately 1nsec as shown in Figure 5(b). We observed that other sources also follow a similar pattern. Figure 6 shows the change in the maximum eigenvalue, λ, of the matrix $\boldsymbol{\Upsilon}$ with frequency. Since λ is a measure of the detectability of the tumor, we can conclude that the best detectability is obtained when $\omega = 0$Hz, where ω is the modulation frequency.

5. CONCLUSION

Optimum distribution of source power is investigated through 2D FEM based simulations. It has been observed that more power should be emitted by the sources where emitted photons traverses the longest path through an absorbing heterogeneity. The effect of tumor location, tumor size, and the number of sources and detectors on the detectability is investigated. When SNR of the test statistics combined with linear detectors and additive

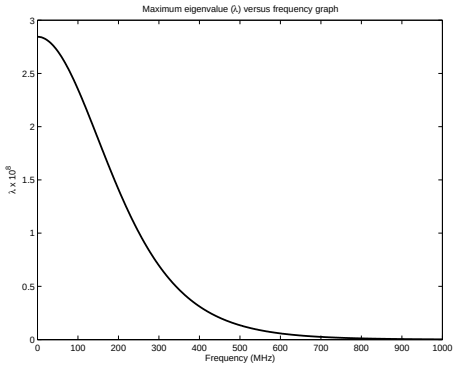

Figure 6. Maximum eigenvalue, λ, versus frequency graph

white noise assumption is used, the detectability criterion is given by the maximum eigenvalue of the difference of source-to-detector maps when heterogeneity is present and absent. The optimum multi-frequency waveforms are also designed with respect to the same detectability criterion. The effect of modulation frequencies on the detectability of tumor presence is investigated. It has been observed that more power should be concentrated on the direct-current component ($\omega = 0$Hz) of the continuous-time waveform.

In this work, the diffusion coefficient, D, is assumed to be constant throughout the domain. However, the framework introduced can be used to investigate the the concurrent effects of absorption and diffusion perturbations on tumor detectability and image quality. Similarly, this framework can be used to investigate optimal choice of wavelengths to maximize detectability. In this work, we assume that the absorption coefficients are deterministic and known. However, in practice, they are unknown quantities. When statistical information on the optical properties of the medium is known, the framework can be extended to design optimum source vector for unknown media.

REFERENCES

1. D. Piao, S. Jiang, H. Dehghani, S. Srinivasan, and B. W. Pogue, "Instrumentation of rapid near-infrared diffuse optical tomography for imaging of tissue at 35 frames per second," in Proc. of 2006 SPIE Photonic West, San Jose, California USA, January 21-26, 2006, in print.
2. C. H. Schmitz, H. L. Graber, H. Luo, I. Arif, J. Hira, Y. Pei, A.Y. Bluestone, S. Zhong, R. Andronica, I. Soller, N. Ramirex, S. L. S. Barbour, R. L. Barbour, "Instrumentation and calibration protocol for imaging dynamic features in dense-scattering media by optical tomography," Appl. Opt. **39**, 6466-6486 (2000).
3. T. O. McBride, B. W. Pogue, S. Poplack, S. Soho, W. A. Wells, S. Jiang, U. Osterberg, and K. D. Paulsen, "Multispectral near-infrared tomography: a case study in compensating for water and lipid content in hemoglobin imaging of the breast," J. Biomed. Opt. **7**, 7279 (2002).
4. H. Dehghani, B. Pogue, S. Poplack, and K. Paulsen, "Multiwavelength Three-Dimensional Near-Infrared Tomography of the Breast: Initial Simulation, Phantom, and Clinical Results ," Appl. Opt. **42**, 135-145 (2003).
5. A. Dunn, A. Devor, H. Bolay, M. Andermann, M. Moskowitz, A. Dale, and D. Boas, "Simultaneous imaging of total cerebral hemoglobin concentration, oxygenation, and blood flow during functional activation," Opt. Lett. **28**, 28-30 (2003).
6. Frederic Bevilacqua, Andrew J. Berger, Albert E. Cerussi, Dorota Jakubowski, and Bruce J. Tromberg, "Broadband Absorption Spectroscopy in Turbid Media by Combined Frequency-Domain and Steady-State Methods," Appl. Opt. **39**, 6498-6507 (2000).
7. A. Corlu, R. Choe, T. Durduran, K. Lee, M. Schweiger, S. Arridge, E. Hillman, and A. Yodh, "Diffuse optical tomography with spectral constraints and wavelength optimization," Appl. Opt. **44**, 2082-2093 (2005).

8. E. Graves, J. Culver, J. Ripoll, R. Weissleder, and V. Ntziachristos, "Singular-value analysis and optimization of experimental parameters in fluorescence molecular tomography," J. Opt. Soc. Am. A **21**, 231-241 (2004).
9. H. Xu, H. Dehghani, and B. W. Pogue, "Near-infrared imaging in the small animal brain: optimization of fiber positions," J. Biomed. Opt. **8**, 102-110 (2003).
10. S. Oh, A. Milstein, R. Millane, C. Bouman, and K. Webb, "Source-detector calibration in three-dimensional Bayesian optical diffusion tomography," J. Opt. Soc. Am. A **19**, 1983-1993 (2002).
11. V. Ntziachristos, A. G. Yodh, B. Chance, "Optical tomography using multi-frequency intensity information," Engineering in Medicine and Biology, 1999. 21st Annual Conf. and the 1999 Annual Fall Meeting of the Biomedical Engineering Soc. BMES/EMBS Conference, 1999. Proceedings of the First Joint Volume 2, 13-16 Oct. 1999 Page(s):1100 vol.2
12. A. Milstein, "Imaging of near-infrared fluorescence, absorption, and scatter in turbid media," Ph.D. Thesis, Purdue University, August 2004.
13. D. Isaacson, "Distinguishability of conductivities by electric current computed tomography," IEEE Trans. Med. Imag., vol. MI-5, pp. 91-95, 1986.
14. M. Cheney, D. Isaacson, J. C. Newell, S. Simske, and J. Goble, "NOSER an algorithm for solving the inverse conductivity problem," Int. J. Imag. Syst. Technol., vol. 2, pp. 66-75, 1990.
15. M. Cheney and D. Isaacson, "Distinguishability in impedance imaging," IEEE Trans.n Biomed. Imag., vol. 39, no. 8, pp. 852-860, Aug. 1992.
16. E. Demidenko, A. Hartov, and K. Paulsen, "Statistical estimation of resistance/conductance by electrical impedance tomography measurements," IEEE. Trans. Med. Imag., vol. 23 (7), pp. 829-838, July 2005.
17. S. M. Kay, *Fundamentals of Statistical Signal Processing, Vol 2: Detection Theory*, (1998) Prentice Hall Signal Processing Series.
18. S. R. Arridge, 1995 Photon Measurement Density Functions Part 1: Analytical Forms *Appl. Opt.* **34** 7395–409.
19. Gilbarg and Trudinger, *Second order elliptic partial differential equations.*
20. S. C. Brenner, and L. R. Scott, *The mathematical theory of finite element methods*, Springer, Berlin, 1994.
21. H. Barrett and K. J. Myers, *Foundations of Image Science*, (2004) John Wiley and Sons Inc. Publications.
22. "Laser Exposure Limits & Hazard Calculations," OSHA Technical Manual, Chapter 6: Laser Hazards.